Smart Materials in Medicine 4 (2023) 552–561

Contents lists available at ScienceDirect

Smart Materials in Medicine

journal homepage: www.keaipublishing.com/en/journals/smart-materials-in-medicine/

Chitosan-calcium carbonate scaffold with high mineral content and hierarchical structure for bone regeneration

Xiaoyang Liu, Zhengke Wang *

MOE Key Laboratory of Macromolecular Synthesis and Functionalization, Department of Polymer Science and Engineering, Zhejiang University, Hangzhou, Zhejiang Province, 310058, China

ARTICLE INFO

Keywords:
Chitosan
Calcium carbonate
Mineralization
Hierarchical structure
Bone regeneration

ABSTRACT

Bone regeneration scaffolds loaded with osteoblast-related cells or cytokines exhibit outstanding therapeutic potential during large-scale bone defect repair. However, limited sources of cells, opportune choosing of growth factors and their concentration, as well as immunological rejection, seriously hinder its clinical application. Developing a scaffold that can effectively recruit MSCs *in situ* and achieve endogenous bone regeneration is a viable strategy. Herein, we report a chitosan-calcium carbonate scaffold with high mineral content and centripetal pore arrangement using a simple *in situ* mineralization method. *In vivo* results first time demonstrate that the scaffold with high calcium carbonate content can effectively recruit MSCs near the defect area, induce their osteogenic differentiation, and ultimately accelerate the process of bone regeneration. Considering the accessible preparation and excellent osteogenicity, the chitosan-calcium carbonate scaffold possesses high potential for the therapeutics of massive bone defects.

1. Introduction

Bone exhibits extraordinary mechanical properties thanks to its high mineral content and complicated structure [1]. During its normal life, some transient or narrow bone fractures can generally be repaired without any external assistance. Despite that, congenital bone malformations, chronic inflammation, serious trauma, and clinical resection of malignant bone tumors can all result in large bone defects that exceed the ceiling of spontaneous healing [2]. Such severe bone defects present huge challenges for both patients and orthopedic surgeons. Although autograft is still the gold standard for bone defect repair, its innate drawback of limited donors has prompted researchers to continuously develop suitable synthetic bone repair materials including bone cement, hydrogels [3,4], scaffolds [5], ceramics [6], and metals [7]. Complicated prosthetic environments require implants with versatile capacities: biocompatibility, osteoinductivity, osteoconductivity, excellent mechanical property, and preferably antibacterial activity [8].

As a natural cationic polysaccharide, chitosan is widely used as dental, bone, or cartilage implants since its versatility includes non-toxic, non-allergenic, mucoadhesive, biocompatible, biodegradable properties [9,10]. However, the poor osteoinductivity restrains its application in large-scale bone regeneration. The introduction of inorganic matter in the chitosan matrix, especially for calcium-containing mineral salts, is a promising way [11]. To date, numerous studies have chosen to introduce hydroxyapatite into the scaffolds to promote the bone repair process [12–14]. Although hydroxyapatite is widely present in nature as the main inorganic constituent of bone, synthetic hydroxyapatite differs from natural hydroxyapatite in size, morphology, crystallinity, and element doping, which results in a low degradation rate as a calcium source and phosphorus source [15,16]. In contrast, the research on the bone regeneration effect of calcium carbonate, which was also widely present in nature, was much less. Scientists seem to be keener to investigate and mimic the calcium carbonate-related "brick-and-mortar" structure in shells [17,18]. Surprisingly, a study indicated that $CaCO_3$ was more effective in supporting the osteogenesis of bone marrow mesenchymal stem cells (MSCs) than hydroxyapatite, particularly in the early stage [19].

With the deepening of research on bone repair scaffolds, researchers noticed that compared with disordered porous scaffolds, the scaffolds with oriented porous structures were more beneficial for the infiltration and migration of osteoblast-related cells, the transfer of nutrients and metabolic wastes, and the formation of extracellular matrix [20–22]. Wang et al. prepared axially oriented osteoconductive mineralized hydrogel through natural pine wood as a template to induce bone

* Corresponding author.
E-mail address: wangzk@zju.edu.cn (Z. Wang).

https://doi.org/10.1016/j.smaim.2023.04.004
Received 21 December 2022; Received in revised form 17 April 2023; Accepted 19 April 2023
Available online 28 April 2023

formation and enhance osteointegration [23]. Nevertheless, unidirectional scaffolds exhibit poor osteogenic potential when used not in long-bone defect models, but in lacunar bone defects or skull defects. In these situations, the monodirectional cellular structure seems to be undesirable for migration and infiltration of MSCs and osteoblasts since the absence of lateral open pore structure [24]. To this end, radially centripetal microporous scaffolds with sufficient side holes are expected to be more advisable for these cases. With the help of radial freeze-casting technology, Wu et al. achieved osseointegration, osteogenesis, and angiogenesis simultaneously in a cranium defect model by using concentric porous scaffolds without any additional growth factors or stem cells [25]. Similarly, Jiang et al. constructed a scaffold with a radially oriented porous structure to accelerate the movement and infiltration of vicinal bone-regeneration-related cells, while preventing the invasion of non-osteoblasts and fibroblasts along its lengthwise direction, guaranteeing a healthy bone regeneration process [24]. Unfortunately, simple blending followed by freeze casting could not guarantee a uniform dispersion of inorganic minerals in the matrix. Achieving precise temperature control during freeze casting by liquid nitrogen seems to be ponderous. It remains a challenge to develop a simple but effective strategy to achieve a uniform dispersion of minerals while ensuring the scaffold possesses a radially porous structure.

Herein, we developed a chitosan/$CaCO_3$ scaffold with high mineral content and centripetal pore arrangement by a simple *in situ* mineralization method. As expected, $CaCO_3$ was uniformly dispersed in chitosan matrix in the form of calcite. The radially centripetal microporous structure of the scaffold was achieved through the synergy of ion diffusion in the gelation process and the extension of ice crystals within the freezing process. The results of animal experiments first time indicated that the scaffold with high calcium carbonate content and concentric microporous structure could efficiently recruit MSCs near the defect area, and ultimately accelerated bone regeneration. This scaffold with high mineral content and special structure will provide great potential for bone regeneration.

2. Experimental section

2.1. Materials

Chitosan (degree of deacetylation: 90%, Mw = 200,000) was supplied by Qingdao Hecreat Bio-tech Company Ltd (Qingdao, China). Calcium acetate was provided by Shanghai Yien Chemical Technology Co., Ltd. The rest of chemicals and reagents like sodium hydroxide, acetic acid, and sodium carbonate et al. were all supplied by Sinopharm Chemical Reagent Co., Ltd and were applied without further purification. The deionized water was provided by Zhejiang University.

2.2. Fabrication of CS/$CaCO_3$ scaffold

The CS/$CaCO_3$ scaffold was developed using a simple *in situ* mineralization method for uniform distribution of the inorganic phase [26]. Under vigorous agitation, CS and calcium acetate were dissolved in 2% acetic acid solution in different proportions, and allowed to stand overnight until degas. Having formed a layer of gel film over the outer layer of chitosan solution with an alkaline solution, it was immersed in a coagulation bath rich in OH^- and CO_3^{2-}. Gelation and mineralization of the solution occur simultaneously using the ionic diffusion effect of hydroxide and carbonate, and a stratified structure was formed. After that, the hydrogel was soaked repeatedly to remove excess ions, and the CS/$CaCO_3$ scaffold was obtained by freeze-drying. Based on the mineral content of the system, scaffolds were divided into four groups, namely Chitosan, $CaCO_3$ 20%, $CaCO_3$ 40%, and $CaCO_3$ 60%.

2.3. Characterization of scaffolds

The FTIR spectra of the scaffolds were measured on an attenuated total reflection-FTIR spectroscope (Nicolet 6700, Thermo, American), and the scanned wavenumber ranged from 4000 to 500 cm^{-1}. The XRD patterns were acquired with X-ray diffractometer (Ultima IV, Rigaku Corporation, Japan) operated at 40 kV, 30 mA, and 20 °C. The thermogravimetric curves of different scaffolds were obtained through a thermogravimetric analyzer (TA-Q500, TA Instruments, American) from 25 °C to 850 °C, using a heating rate of 10 °C/min and oxygen atmosphere. The scaffolds were sprayed with platinum and observed by a scanning electron microscope (S-4800, Hitachi, Japan) with different magnifications. The porosity of the scaffold was determined by the ethanol displacement methodology. Using the mechanical universal testing machine (5543 A, Instron, China) to measure the compressive mechanical properties of scaffolds under a compression speed of 1 mm/min. Five specimens for each group with different $CaCO_3$ content were tested. We define the yield point as the compressive strength and the average modulus for the first 10% strain as the compressive modulus.

2.4. In vitro migration assay

The CS/$CaCO_3$ scaffolds with different $CaCO_3$ content were placed into the bottom of 24-well plates, and the wells were divided into upper and lower parts by the corresponding Transwell chambers (pore size: 8 μm, Corning, USA). MSCs were seeded on the upper chambers with a density of 2×10^4 cells/ml. After 24 h of cultivation, the cells in the upper layer of the semi-permeable membrane were gently erased away with a cotton swab. The MSCs that penetrated to the other side of the membrane were immobilized with 4% paraformaldehyde and stained with crystal violet solution at 0.5% concentration. Images were taken with an inverted microscope (Axio Observer 7, Zeiss).

2.5. In vitro osteogenic evaluation

The osteogenic induction medium was composed of DMEM, 10% fetal bovine serum (FBS, Gibco), 1% penicillin-streptomycin (Gibco), 10 mM β-glycerol phosphate (Sigma-Aldrich), 200 μM ascorbic acid (Sigma-Aldrich) and 100 nM dexamethasone (Sigma-Aldrich). MSCs (OriCell® Wistar) were seeded in 24-well plates with a concentration of 2×10^4 cells/mL and cultured with osteogenic induction medium (replaced every 48 h).

The alkaline phosphatase (ALP) activity was evaluated on Day 7 after inducing osteogenesis with the scaffolds in osteoinductive medium. To assess the ALP activity quantitatively, cells were lysed by RIPA lysis buffer (Beyotime), and the supernate was collected by centrifugation (14,000 r/min) at 4 °C. The total protein and ALP expression were measured by BCA assay kit and *p*-nitrophenyl phosphate (PNPP) assay kit according to the instructions. The optical density that reflected the ALP activity and total protein expression was measured by a microplate reader (Varioskan™ LUX, Thermo Fisher) at 490 nm and 595 nm.

Alizarin red staining (ARS) was carried out to assess the formation of mineralized nodules on Day 7 after co-culture with scaffolds. At the indicated times, cells were fixed with paraformaldehyde and stained with alizarin red solution (1%, PH = 4.1) for 20min. The exceed ARS was washed with deionized water and the staining cells were photographed under an inverted microscope. For the further semi-quantitative analysis of the mineralized nodules, all nodules were dissolved with 10% w/v cetylpyridinium chloride solution and quantified at 562 nm using a microplate reader. In order to eliminate the interference of the minerals released from scaffolds on alizarin red staining, we set up a series of blank control groups that cultured without any cells, and the other steps were completely the same as those of the experimental group. The final quantitative analysis was performed after eliminating the distraction of minerals released from the scaffolds.

2.6. In vivo MSCs recruitment assessment

The capacity of CS/$CaCO_3$ scaffold to recruit host MSCs *in vivo* was

assessed using immunofluorescence staining [27]. Briefly, scaffolds with different $CaCO_3$ content were embedded in a 5-mm defect created in the calvarium of rats. One week after implantation, scaffolds were removed and submerged in DMEM. Cells in the scaffolds were harvested and labeled with CD29 Monoclonal Antibody-FITC (eBioscience™) and CD45 Monoclonal Antibody-APC (eBioscience™). The obtained labeled cell suspensions were analyzed by flow cytometry.

To visually evaluate the MSCs recruitment effect, the scaffolds implanted *in vivo* were analyzed by immunofluorescence staining. One week after the operation, different scaffolds were taken out and fixed in 4% paraformaldehyde. Frozen sections (10 μm) of retrieved scaffolds were incubated with 10% FBS for 60 min at 37 °C and then with FITC-labeled CD29 antibody (Merck Millipore Co., USA) and ALEXA 594-labeled CD45 antibody (Bioss Inc., Woburn, MA, USA) at 4 °C overnight. Nuclei were stained by Hoechst 33,258. The stained sections were observed via CLSM. The cells in the implanted scaffolds were identified as MSCs when they were stained positive for the mesenchymal marker CD29 (green) and negative for the hematopoietic marker CD45 (red).

2.7. Bone regeneration assessment

All procedures related to animal feeding and surgery were conformed with the relevant laws and authorized by the Institutional Animal Care and Use Committee (reference number: ZJCLA-IACUC-20140001). A critical-sized bone defect model of rat skulls was chosen to evaluate the impact of the mineral content and centripetal porous structure in scaffolds on bone regeneration. Thirty mature and healthy rats (220 g, n = 5 for each group, 10 rats for MSCs recruitment, and the remaining rats were used for bone regeneration for 6 weeks and 12 weeks, respectively) were used in this study. All animals received feed and water without restriction and were accommodated at 25 °C with a steady light/dark cycle. Rats implanted with different scaffolds were narcotized intraperitoneally with pentobarbital. After shaving the head fur, a longitudinal slit was created to incise the skin and subcutaneous tissue successively. The residual tissues and blood vessels on the surface of the skull were completely removed with 30% hydrogen peroxide and the periosteum covering the cranial bone was completely excised. Two full-thickness, 5-mm, critical-sized bone defects were created using a corneal trephine in one rat. Then, chitosan, $CaCO_3$ 20%, $CaCO_3$ 40%, and $CaCO_3$ 60% scaffolds were casually chosen to embed the skull defect in these rats. After the surgery, antibiotic prophylaxis was continued for 3 days, and animals were allowed free movement in the cage. At 6 and 12 weeks after operation, 10 rats with different scaffolds were euthanized via overdose of pentobarbital sodium. The defect sites were identified, resected, and fixed in 10% formalin fixative for further testing. To evaluate the new bone formation, microcomputed tomography (U-CT-XUHR micro-CT, Milabs, Holland) was used to collect relevant data and reconstructed 3D images. Furthermore, we analyzed the mineralization process, the degradation of scaffolds, and the fibrous tissue formation in the defect area through H&E and Masson's trichrome staining techniques.

Statistical analysis: All data were presented in the form of mean ± standard deviation and analyzed by SPSS software. One-way ANOVA was chosen for the significance test between different groups, and the statistical significance was defined as $p^* < 0.05$, $p^{**} < 0.01$.

3. Results and discussion

3.1. Physical properties of CS/$CaCO_3$ scaffolds

We carried out FTIR, XRD, and TGA spectra to confirm the mineralization of $CaCO_3$ in CS scaffolds with preset content. As shown in Fig. 1A, the FTIR spectra exhibited representative calcium carbonate-like

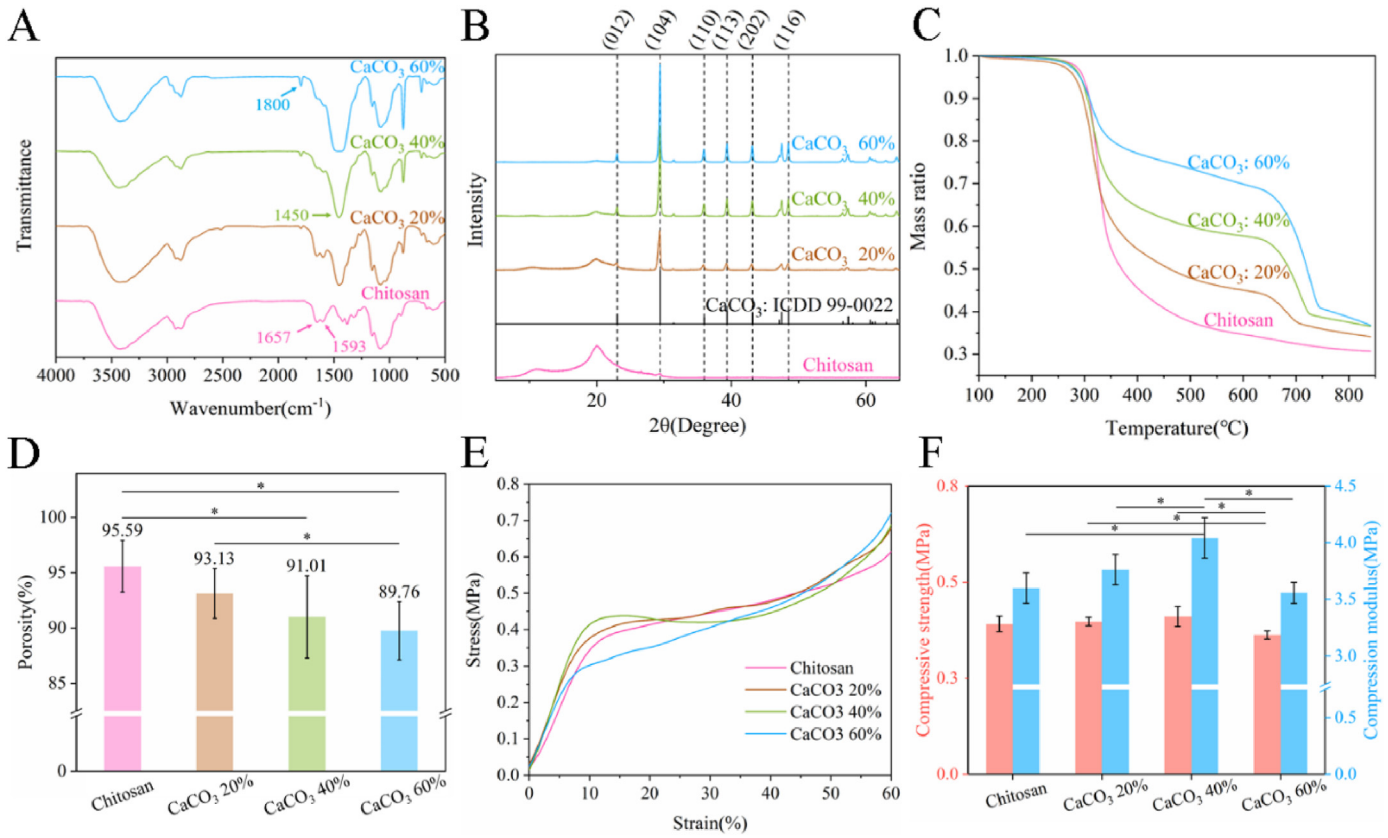

Fig. 1. Composition, porosity, and mechanical properties of CS/$CaCO_3$ scaffolds. **(A)** FTIR spectra and **(B)** XRD analysis showed the typical absorption peaks and characteristic crystal planes of $CaCO_3$ in hybrid scaffolds. **(C)** TGA results confirmed the $CaCO_3$ content in scaffolds as designed. **(D)**The porosity of different scaffolds measured by ethanol displacement methodology. **(E)**Compression curves of scaffolds. **(F)** Compression strength (orange) and compression modulus (blue) of scaffolds.

vibration peaks. The absorption peaks appeared at 1657 cm^{-1} and 1593 cm^{-1} contributed to the amide I and amide II of CS. And the broad peak ranged from 3500 to 3300 cm^{-1} due to –OH and $–NH_2$ in CS matrix. The vibration peaks appeared near 875 cm^{-1}, which represented the main characteristic peaks of CO_3^{2-}, were gradually strengthening with increasing $CaCO_3$ content. Likewise, the relative intensity of the absorption peaks at 1450 and 1800 cm^{-1} which were related to the stretching vibration of *C*–O were increasing. The XRD results in Fig. 1B demonstrated the incorporation of calcium carbonate in CS scaffolds. The sharp crystalline peaks were deeply conformable with standard PDF card 99–0022 of $CaCO_3$. From the TGA spectra (Fig. 1C), it could be easily confirmed that the $CaCO_3$ contents, which remained stable at 600 °C, were 0%, 22.07%, 41.23%, and 60.64% for Chitosan, $CaCO_3$ 20%, $CaCO_3$ 40%, and $CaCO_3$ 60% scaffolds, respectively.

For tissue engineering, the structural characteristics, especially for the pore geometries like pore volume, form, mutual connectivity, and the arrangement of pores of the scaffolds could significantly influence cell adhesion, proliferation, and tissue regeneration [28]. High porosity around 80–90% was promising to realize practical cell movement and proliferation throughout the scaffolds [29]. In this research, all scaffolds contained high porosity after freeze-drying. Although the introduction of large amounts of $CaCO_3$ decreased the porosity of the scaffolds, it

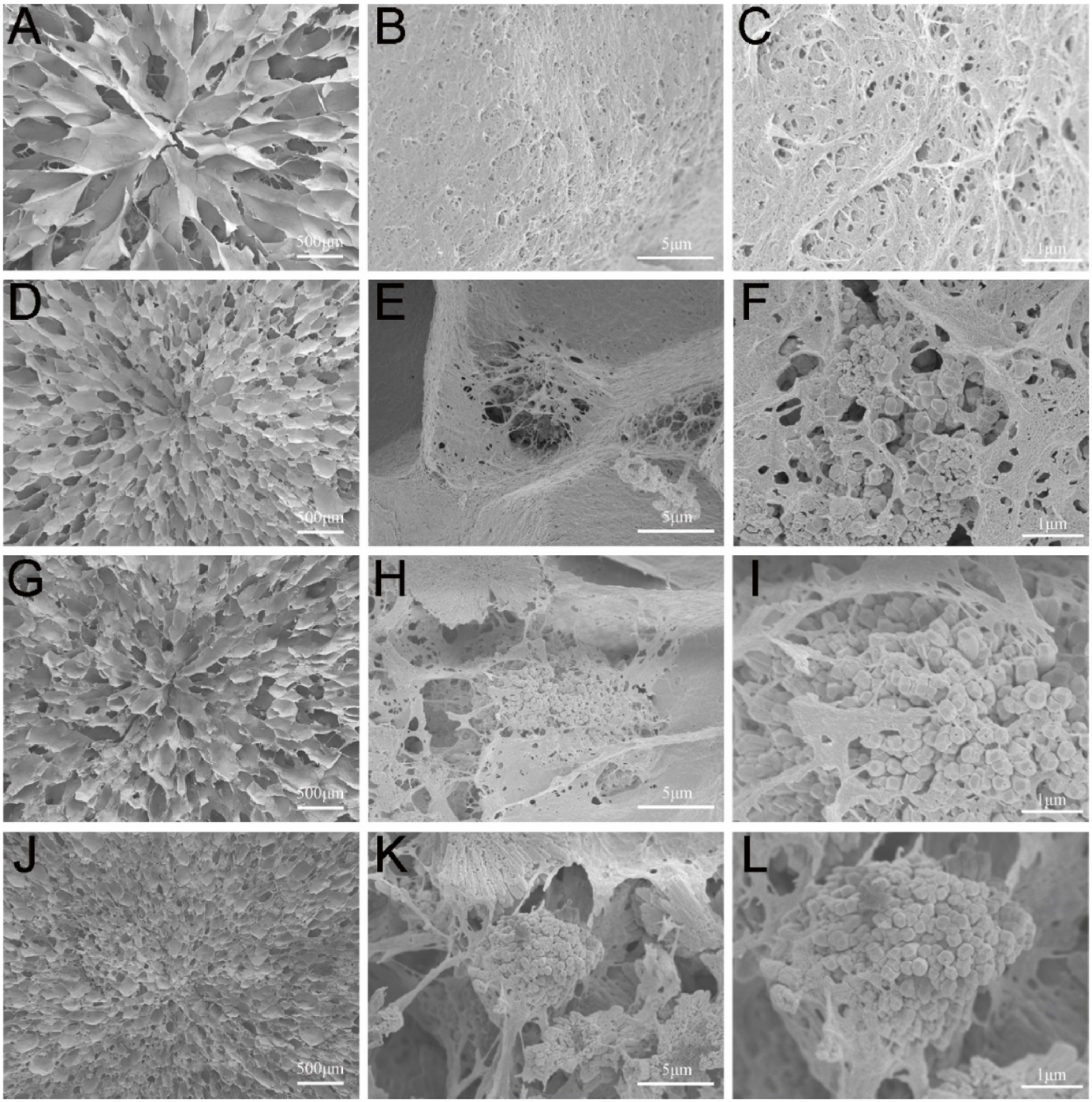

Fig. 2. SEM images of CS/$CaCO_3$ scaffolds. (**A**), (**B**), and (**C**) SEM images of Chitosan scaffold: × 30, × 10,000, × 20,000; (**D**), (**E**), and (**F**) SEM images of $CaCO_3$ 20% scaffold: × 30, × 10,000 and × 20,000; (**G**), (**H**), (**I**) SEM images of $CaCO_3$ 40% scaffold: × 30, × 10,000, × 20,000; (**J**), (**K**), (**L**) SEM images of $CaCO_3$ 60% scaffold: × 30, × 10,000, × 20,000.

remained nearly 90% with 60% $CaCO_3$ content (Fig. 1D). Sufficient pores ensured the attachment and propagation of bone-related cells, thereby accelerating the repair process of bone defects. In addition, the course of bone regeneration is often carried out under external force. Scaffolds, especially for bone repair, are needed to guarantee sufficient mechanical support for cells while maintaining porosity. Furthermore, a hard matrix was more beneficial for the differentiation of MSCs towards osteoblasts [30]. The representative stress-strain curves were depicted in Fig. 1E. All the scaffolds performed analogous stress-strain behavior, and the higher content of $CaCO_3$ led to a better compressive performance in the early stage. When $CaCO_3$ content reached 60%, the compressive strength and modulus of the scaffolds did not increase but decreased to be comparable to pure chitosan which could be ascribed to the agglomeration and phase separation in scaffolds due to excessive calcium carbonate content.

The structural features of scaffolds had been demonstrated to be significant for modulating cell behavior, mineral deposition, tissue regeneration, and vascularization [31]. As illustrated in Fig. 2, under low magnification, all kinds of mineralized scaffolds displayed a hierarchical network architecture consisting of radial channels and interlinking open holes from the midst to the verge. Interestingly, these sophisticated, centripetal, and porous structures were prepared by simple *in situ* mineralization and freeze-drying. The ion diffusion during the CS gelation process and the ice crystal growth caused by the temperature gradient during the freezing process jointly brought up the complex structure of the scaffolds [26]. Research proved that these radially oriented conduits and interlinking open pores structures would be effectual in supporting the extensive invasion of osteoblast and angioblast, eventually leading to rapid endogenous bone regeneration [25].

Pores in scaffolds play a vital role in tissue regeneration. Macropores (>50 μm) were beneficial to cell adhesion and proliferation, while micropores (<50 μm) could impede protein adsorption onto the scaffolds [32]. Various cells prefer various pores with different sizes: chondrocyte and osteoblast prefer pore sizes from 380 to 405 μm, while fibroblast tends to access 186–200 μm pore size. For new bone generation, voids in 290–310 μm might be favorable [33]. In this research, holes in scaffolds exhibited a centripetal fusiform morphology rather than traditional circular morphology. As shown in Fig. S2, the size of the voids gradually decreased with increasing $CaCO_3$ content, from 512.35 ± 63.12 μm for CS scaffold to 215.62 ± 37.33 μm for $CaCO_3$ 60% scaffold.

Besides pore size, the roughness of scaffolds could also regulate cell behavior. It was demonstrated that rough or even surfaces induced different cell responses, for example, periodontal fibroblast cells attached stronger to smoother surfaces, epithelial cells usually adhered to a flat substrate, while osteoblast cells preferred rougher surfaces [34]. Fig. 2A and B indicated that pure CS scaffold possessed a smoother surface than others. The introduction of $CaCO_3$ effectively increased the roughness of

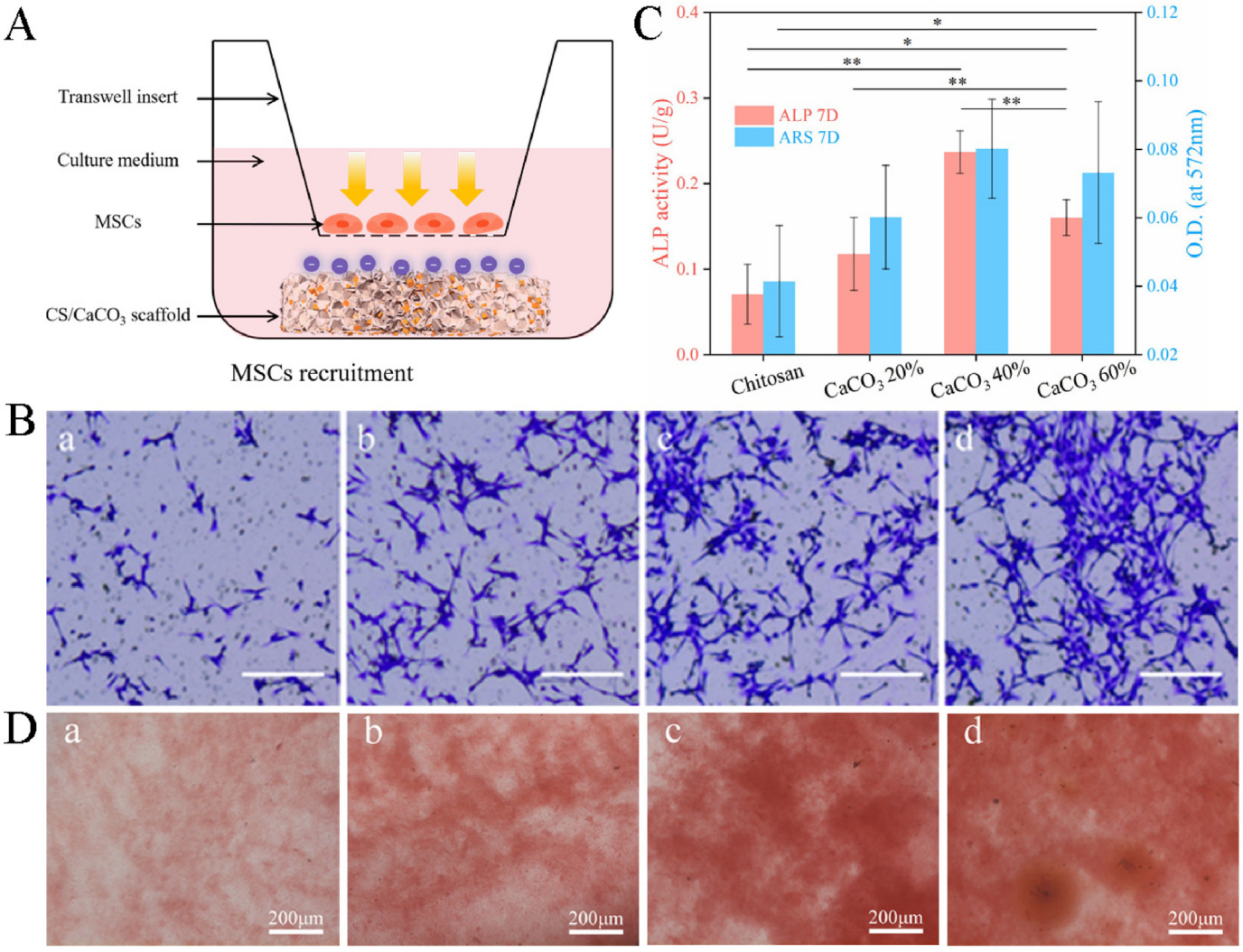

Fig. 3. MSCs migration and osteogenic differentiation in vitro. (A) Schematic illustration of MSCs migration assay; (B) MSCs migration induced by different scaffolds after 24 h: (a) Chitosan, (b) $CaCO_3$ 20%, (c) $CaCO_3$ 40%, and (d) $CaCO_3$ 60%, scale bar = 200 μm; (D) Alizarin red staining after 7 days of induction: (a) Chitosan, (b) $CaCO_3$ 20%, (c) $CaCO_3$ 40%, and (d) $CaCO_3$ 60%.

the scaffolds. According to the energy dispersive spectroscopy (EDS), $CaCO_3$ was uniformly dispersed in CS matrix (Fig. S3 and Fig. S4). We compared scaffolds with different $CaCO_3$ content from 0 to 60% and found that with the increase of inorganic content, some $CaCO_3$ aggregates gradually appeared but the overall distribution of calcium on the scaffold was uniform. The favorable dispersion was also demonstrated by TEM images of dried samples of chitosan hydrogel containing 15% $CaCO_3$. The uniform dispersion of $CaCO_3$ crystal in chitosan matrix was attributed to the dense network of chitosan molecules and the blocking effect of high viscosity on Ca^{2+} (Fig. S1).

3.2. MSCs migration and osteogenic differentiation in vitro

Here, we assessed the effect of CS/$CaCO_3$ scaffolds on the migration of MSCs through the Transwell invasion assay (Fig. 3A). As shown in Fig. 3B, there were marked differences between scaffolds with different $CaCO_3$ contents on the migration of MSCs. With the increase of the $CaCO_3$ content, more MSCs migrated to the lower chamber. In the physiological environment, the ζ-potential of $CaCO_3$ was usually negative, especially in the case of proton capture by chitosan [35]. In contrast, MSCs possessed membranes whose outer surface was positive potential while the inner showed negative [36]. The potential difference between $CaCO_3$ crystals and MSCs cell membrane might be the main driving force to attract MSCs.

One of the crucial criteria for evaluating bone repair scaffolds was their capacity to induce osteogenic differentiation of cells. We co-cultured MSCs with CS/$CaCO_3$ scaffolds containing different $CaCO_3$ contents and evaluated the osteogenic potential of the scaffolds by ALP activity analysis and Alizarin red staining. The results of the quantitative analysis of ALP protein indicated that $CaCO_3$ 40% scaffold exhibited optimal osteogenic induction potential (Fig. 3C). The release of Ca^{2+} from scaffolds contributed to the osteogenic differentiation of MSCs, which was consistent with many literatures on the promotion of osteogenesis by materials containing $CaCO_3$ [19,37].

Similar to the ALP activity test results, cells co-cultured with CS/$CaCO_3$ 40% scaffold secreted the most mineralized nodules as shown in Fig. 3C and D. Based on the image of alizarin red staining alone (Fig. 3D), both scaffolds with $CaCO_3$ content of 40% and 60% showed high production of minerals. However, when the mineral background released by different scaffolds was removed, the mineral production of CS/$CaCO_3$ 40% scaffold was significantly higher than that of CS/$CaCO_3$ 60% scaffold (Fig. 3C). Pure chitosan could not effectively induce the osteogenic differentiation of MSCs since the lack of active components. Besides external chemical stimulation, the mechanical properties of the matrix could also effectively modulate the osteogenic differentiation of cells [38]. CS/$CaCO_3$ 60% scaffold possessed the highest $CaCO_3$ content, while its osteoinductive performance was only slightly better than that of $CaCO_3$ 20% scaffold, which could be explained by its worst mechanical properties. The small pore size and low porosity caused by the high mineral content were also not conducive to the osteogenic differentiation of MSCs.

3.3. Bone regeneration performance in vivo

Recruiting adjacent stem cells to sites of injury to speed tissue repair was the decisive factor for *in situ* tissue engineering repair without cell

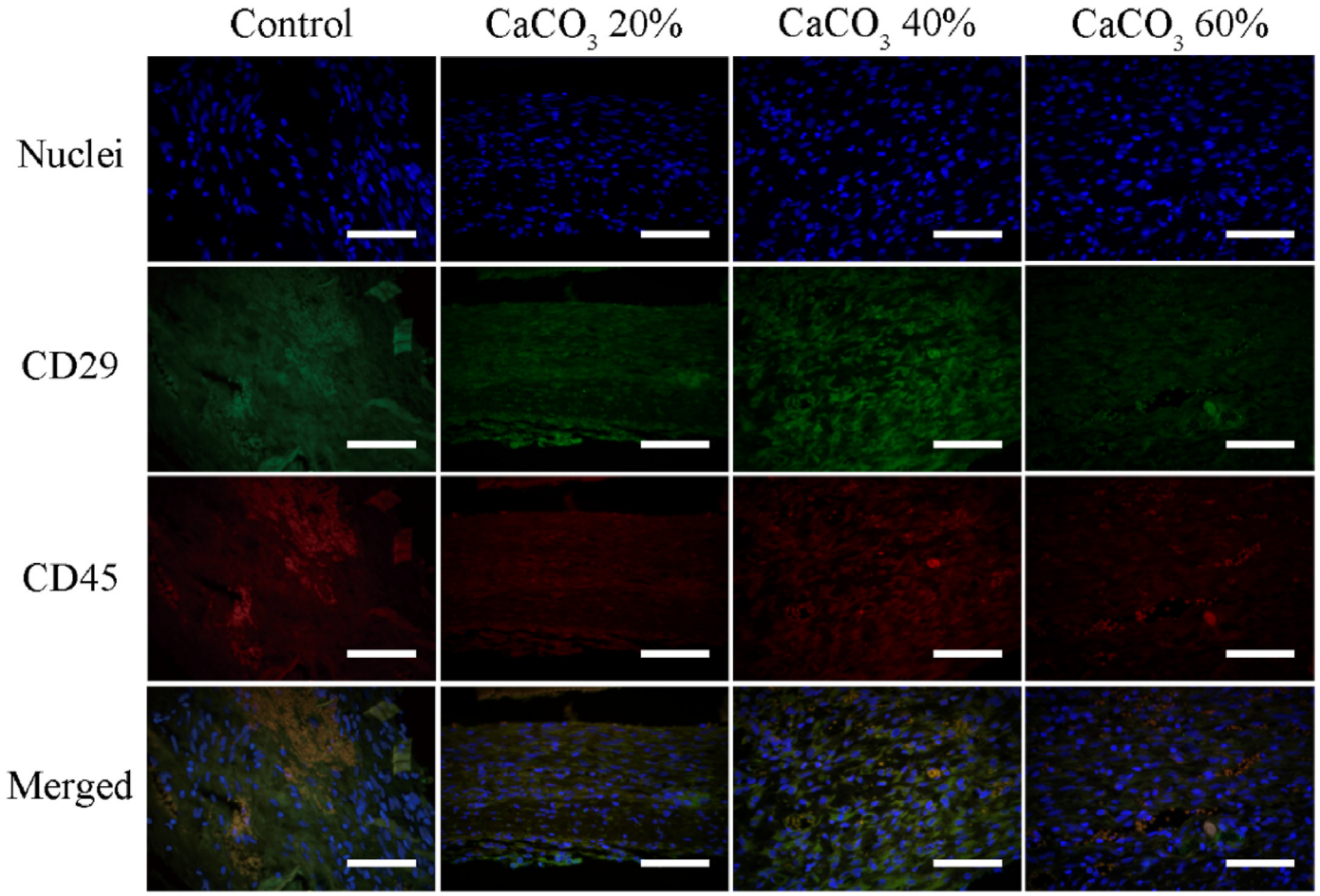

Fig. 4. Immunostaining for the surface markers CD29 and CD45. Cells residing on the implanted scaffolds were identified as MSCs when staining for the mesenchymal marker CD29 was positive while the hematopoietic marker CD45 was negative. (Green: CD29; Red: CD45; Blue: nuclei; scale bar = 300 μm).

loading [39]. Different scaffolds were randomly implanted into the skull defects. We took out all placed scaffolds on Day 7 after surgery. Immunofluorescence assay was used to identify MSCs that were positive for CD29 which was the mesenchymal marker while negative for CD45 which was the hematopoietic marker. Staining results (Fig. 4) showed that endogenous cells with an MSC phenotype ($CD29^{+}$, $CD45^{-}$) existed in all scaffolds except $CaCO_3$ 60% scaffold which might ascribe to its narrow hole. Among scaffolds with different $CaCO_3$ content, $CaCO_3$ 40% performed the best MSCs recruitment effect.

To further quantitatively analyze the MSCs recruitment effect, flow cytometry was used to compare the content of MSCs in different scaffolds. And the results (Fig. S5) indicated that the scaffold with 40% $CaCO_3$ recruited the highest proportion of MSCs which was more than twice the proportion of MSCs recruited by the pure chitosan scaffold. In both immunofluorescence staining and flow cytometry analysis, the $CaCO_3$ 60% group showed the least stem cell recruitment effect, which was probably related to its lower porosity and pore size.

Numerous studies have shown that the recruitment process of MSCs is regulated by a variety of growth factors like SDF-1, IL-3, etc., chemokines including MCP-1/CCL2, RANTES/CCL5, etc., and some soluble factors [40–43]. Furthermore, physical factors such as the morphology and potential of the defect site also have significant effects on the migration of MSCs [36,44]. Hu et al. enhanced the migration of MSC to the injury site through DNA aptamer (Apt) 19 S, promoting biomineralization on

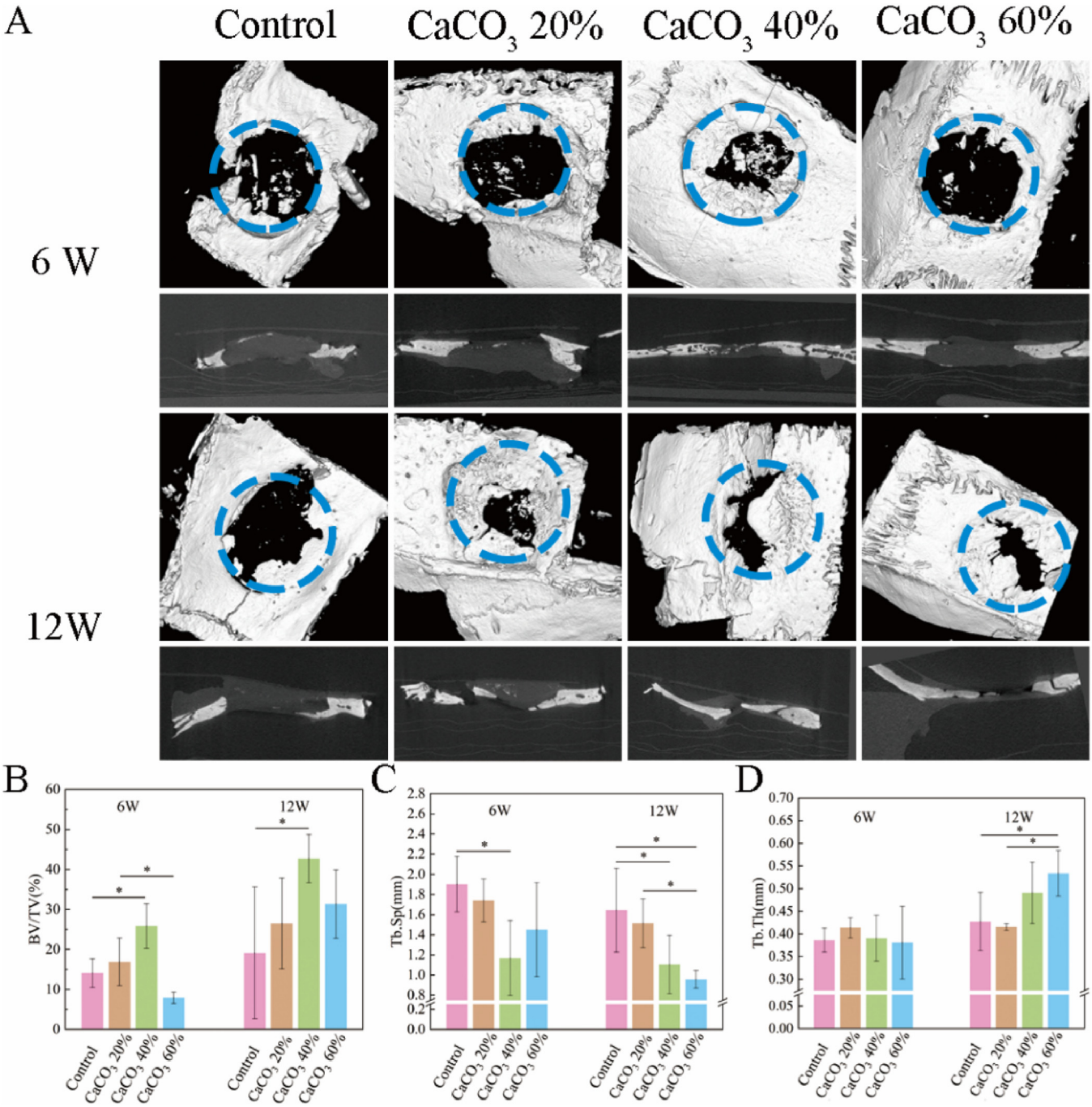

Fig. 5. *In vivo* bone formation using rat calvarial critical size defect model. (**A**) Typical 3D constructed images of horizontal view and coronal view obtained by micro-CT; (**B**) The bone volume/tissue volume (BV/TV), (**C**) trabecular bone separation (Tb. Sp), and (**D**) thickness of trabecular (Tb. Th) were calculated by Imalytics analysis software.

titanium-based implants [36]. Moreover, they pointed out that the prominent electric potential difference between hydroxyapatite and the MSCs which was magnified by *p*-OGP molecules accelerated MSCs to move to the implant surface. From a completely different point of view, Kyung Mi Woo et al. verified that fibrous morphology could achieve the recruitment of MSCs by regulating the transition between the M1 and M2 phenotype of macrophages [44]. Interestingly, Wang et al. compared three types of β-TCP scaffolds composed of traditional cylindrical, cambered gyroid, and complicated diamond pore units respectively, and found that scaffolds with diamond pores were more conducive for MSCs migration and osteogenic differentiation [45]. And they attributed this phenomenon to the intensifying mechanical signal transduction of the RhoA/ROCK2 pathway.

In our work, the driving forces for the recruitment of MSCs could be

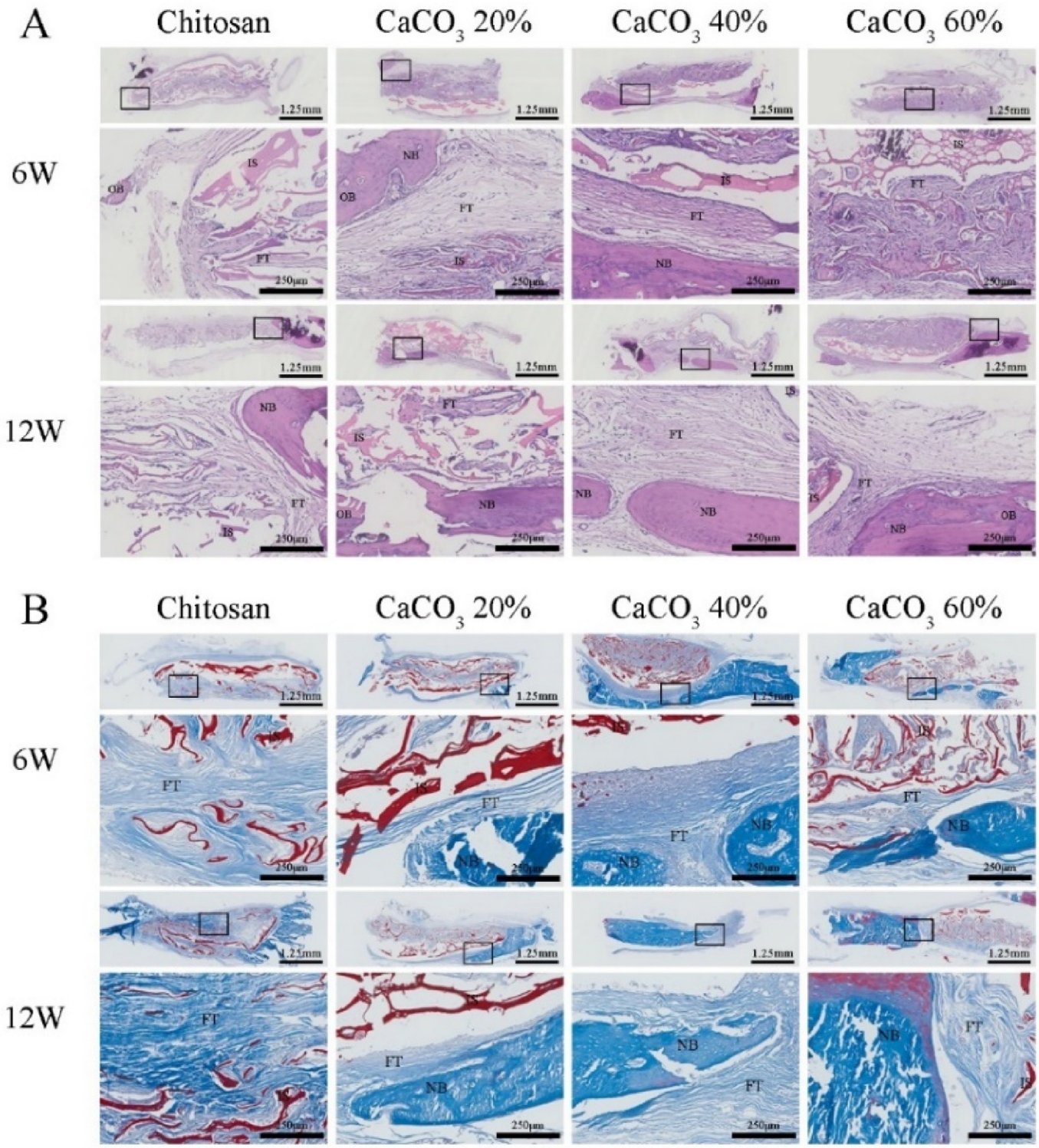

Fig. 6. H&E and Masson's trichrome staining. (**A**) H&E staining; (**B**) Masson's trichrome staining images. (NB: newly formed bone, OB: original bone, FT: fibrous tissue, IS: implanted scaffolds).

divided into two categories: potential and inflammation. As we discussed above, MSCs migrated along the direction of the electric field and finally enriched on the CS/$CaCO_3$ scaffold. Compared with galvanotaxis, the effect of inflammation on the recruitment of MSCs was much more complicated. On the one hand, proinflammatory factors such as IL-1β and TNF-α can enhance the expression of various chemokine receptors in MSCs [43]. On the other hand, excessive inflammatory cytokines could disrupt the existing chemokine concentration gradient, hindering the directional migration of MSCs and bone regeneration [46]. In our scaffolds, chitosan oligomers, as a degradation product of chitosan, could suppress the over-expression of IL-6 and TNF-α in macrophage, which was beneficial to the recruitment of MSCs [47]. Based on the experiment results, we infer that under the premise of ensuring sufficient porosity and pore size of the scaffolds, high content of $CaCO_3$ could recruit more MSCs, which could induce further osteogenesis and new bone formation.

To evaluate the osteogenesis performance of CS/$CaCO_3$ scaffolds *in vivo*, we randomly implanted different scaffolds into the critical bone defect sites of rat calvaria. Since the critical bone defect was difficult to repair by itself [48–50], we chose the CS scaffold group as the control group for evaluation and comparison. At 6 and 12 weeks after surgery, the defect sites were identified, resected, and fixed for further assessment. Both micro-CT scanning and histological staining were chosen to complete an exhaustive evaluation of new bone formation.

As shown in the 3D reconstruction results (Fig. 5A), the bone regeneration degrees of the four scaffold groups were distinct from each other. Among them, the scaffold with 40% $CaCO_3$ content showed the best osteogenesis performance, followed by $CaCO_3$ 60%, $CaCO_3$ 20%, and Chitosan. Quantitative assessment of bone regeneration was realized by Imalytics analysis software, including bone volume/tissue volume (BV/TV), trabecular bone separation (Tb. Sp), and thickness of trabecular (Tb. Th) were performed (Fig. 5B, C, and 5D). After 12 weeks, although there was a slight new bone generation (19.16%) in the CS control group, it was still limited around the edge of natural bone tissue and only formed a thin layer of bone tissue. The introduction of calcium carbonate into the system as an inorganic calcium source could effectively promote bone regeneration, especially for the experimental group with 40% $CaCO_3$ content, which realized the best bone regeneration at 6 W (25.84%) and 12 W (42.74%). In this group, new bone was dense and the thickness is similar to the natural bone. The bone regeneration rate of over 40% was superior to most acellular and drug-free scaffolds and comparable to some drug-loaded scaffolds [5,12,13]. Scaffold with 60% $CaCO_3$ content showed the worst repair effect at 6 W, which might be attributed to its lower porosity and smaller pore size (~200 μm) structural features that were not conducive to the adhesion and proliferation of osteocytes in the initial stage, but with the degradation of the scaffold, it showed a better bone repair effect of 31.36% in 12 W. The Tb. Th in $CaCO_3$ 40% increased from 0.3911 mm (6 W) to 0.4908 mm (12 W), and Tb. Sp decreased from 1.1684 mm (6 W) to 1.1038 mm (12 W), indicating that this scaffold could effectively promote the critical-size bone defect repair process.

Moreover, H&E and Masson's trichrome staining were also analyzed to confirm the radiographic results and to verify the new bone formation. Based on H&E staining results (Fig. 6A), there was little obvious inflammatory reaction, while well-integrated soft tissues were discovered surrounding the inserted scaffolds in all groups, implying favorable biocompatibility of the implanted CS/$CaCO_3$ scaffolds. Consistent with the micro-CT results, varying amounts of newly formed bone tissue (red dense area) were observed in all experimental groups. For the Chitosan group, it was observed that the defect area was dominated by fibrous tissue, with little new bone and a large amount of undegraded scaffold material remaining. In contrast, groups implanted with $CaCO_3$ 40% scaffold induced the most bone tissue after 12 weeks. In Masson's trichrome staining slices, different components could be easily distinguished by color: the tissue rich in collagen fibers like ossified tissue and cartilage were stained blue, while the muscle fibers, and red cells in this area were stained red. The nuclei were stained blue-black (Fig. 6B). For $CaCO_3$ 40% scaffold, there was more collagen deposition and ossification tissue formation than other groups, particularly for Chitosan, which showed predominantly fibrous tissue formation. The staining results suggested that the implantation of $CaCO_3$ 40% scaffold efficiently repaired critical-size bone defects in rats.

4. Conclusions

In summary, we prepared a high-mineral-content scaffold with a special centripetal arrangement structure for bone regeneration through a simple *in situ* mineralization and freeze-drying method. Results indicated that scaffolds with high mineral content similar to natural bone, supplemented by the concentric microporous structure could efficiently recruit MSCs near the defect site, and ultimately accelerated bone regeneration. *In vivo* experiments revealed that increasing the calcium carbonate content in the scaffolds could effectively promote bone regeneration on the basis of moderate porosity and pore size. Unlike the common complex system of introducing growth factors or cells into the scaffolds, our strategy achieved similar bone regeneration effects through simple organic-inorganic composition and special structural design. It would be a manageable and highly efficient therapeutic option in bone tissue engineering and regenerative medicine.

Conflict of interest

The authors declare no conflict of interest.

Data availability statement

The data that support the findings of this study are available from the corresponding author on request.

CRediT authorship contribution statement

Xiaoyang Liu: conducted the experiments, prepared the manuscript. **Zhengke Wang:** designed, supervised the project, revised the manuscript.

Declaration of competing interest

The authors declare that they have no known competing financial interests or personal relationships that could have appeared to influence the work reported in this paper.

Acknowledgments

This work was financially supported by Science Fund for Distinguished Young Scholars of Zhejiang Province (No.LR20E030004), and National Natural Science Foundation of China (No. 51873187).

Appendix A. Supplementary data

Supplementary data to this article can be found online at https://doi.org/10.1016/j.smaim.2023.04.004.

References

[1] T.A. Taton, Nanotechnology - boning up on biology, Nature 412 (2001) 491–492.
[2] J. Zhang, B.Y. Zhang, Z.F. Zheng, Q.Y. Cai, J.C. Wang, Q. Shu, L.J. Wang, Tissue-engineered bone functionalized with MoS2 nanosheets for enhanced repair of critical-size bone defect in rats, Adv. Funct. Mater. 32 (2022).
[3] Z.Y. Zhong, X.D. Wu, Y.F. Wang, M.D. Li, Y. Li, X.L. Liu, X. Zhang, Z.Y. Lan, J.L. Wang, Y.Y. Du, S.M. Zhang, Zn/Sr dual ions-collagen co-assembly hydroxyapatite enhances bone regeneration through procedural osteo-immunomodulation and osteogenesis, Bioact. Mater. 10 (2022) 195–206.
[4] Z.Y. Zou, L. Wang, Z.F. Zhou, Q. Sun, D.L. Liu, Y. Chen, H. Hu, Y. Cai, S.X. Lin, Z.R. Yu, B.Z. Tan, W. Guo, Z.M. Ling, X.N. Zou, Simultaneous incorporation of PTH(1-34) and nano-hydroxyapatite into Chitosan/Alginate Hydrogels for efficient bone regeneration, Bioact. Mater. 6 (2021) 1839–1851.

[5] D.S. Kim, J.K. Lee, J.H. Kim, J. Lee, D.S. Kim, S. An, S.B. Park, T.H. Kim, J.S. Rim, S. Lee, D.K. Han, Advanced PLGA hybrid scaffold with a bioactive PDRN/BMP2 nanocomplex for angiogenesis and bone regeneration using human fetal MSCs, Sci. Adv. 7 (2021).
[6] Y.G. Zhang, J.P. Li, M. Soleimani, F. Giacomini, H. Friedrich, R. Truckenmuller, P. Habibovic, Biodegradable elastic sponge from nanofibrous biphasic calcium phosphate ceramic as an advanced material for regenerative medicine, Adv. Funct. Mater. 31 (2021).
[7] L. Malladi, A. Mahapatro, A.S. Gomes, Fabrication of magnesium-based metallic scaffolds for bone tissue engineering, Mater. Technol. 33 (2018) 173–182.
[8] C.-S. Lee, H.S. Hwang, S. Kim, J. Fan, T. Aghaloo, M. Lee, Inspired by nature: facile design of nanoclay-organic hydrogel bone sealant with multifunctional properties for robust bone regeneration, Adv. Funct. Mater. 30 (2020).
[9] P. Chocholata, V. Kulda, V. Babuska, Fabrication of scaffolds for bone-tissue regeneration, Materials 12 (2019).
[10] W.J. Feng, Z.K. Wang, Biomedical applications of chitosan-graphene oxide nanocomposites, iScience 25 (2022).
[11] X.Y. Liu, Y.X. Wu, X.C. Zhao, Z.K. Wang, Fabrication and applications of bioactive chitosan-based organic-inorganic hybrid materials: a review, Carbohydrate Polym. 267 (2021).
[12] Y.H. Yang, Q. Zhang, T.P. Xu, H.Y. Zhang, M. Zhang, L. Lu, Y.F. Hao, J.Y.H. Fuh, X. Zhao, Photocrosslinkable nanocomposite ink for printing strong, biodegradable and bioactive bone graft, Biomaterials (2020) 263.
[13] Y. Zhao, J.D. Chen, L. Zou, G. Xu, Y.S. Geng, Facile one-step bioinspired mineralization by chitosan functionalized with graphene oxide to activate bone endogenous regeneration, Chem. Eng. J. 378 (2019).
[14] C.J. Shuai, W.J. Yang, P. Feng, S.P. Peng, H. Pan, Accelerated degradation of HAP/PLLA bone scaffold by PGA blending facilitates bioactivity and osteoconductivity, Bioact. Mater. 6 (2021) 490–502.
[15] G. Turnbull, J. Clarke, F. Picard, P. Riches, L.L. Jia, F.X. Han, B. Li, W.M. Shu, 3D bioactive composite scaffolds for bone tissue engineering, Bioact. Mater. 3 (2018) 278–314.
[16] L.C. Palmer, C.J. Newcomb, S.R. Kaltz, E.D. Spoerke, S.I. Stupp, Biomimetic systems for hydroxyapatite mineralization inspired by bone and enamel, Chem. Rev. 108 (2008) 4754–4783.
[17] H.K. Raut, A.F. Schwartzman, R. Das, F. Liu, L.F. Wang, C.A. Ross, J.G. Fernandez, Tough and strong: cross-lamella design imparts multifunctionality to biomimetic nacre, ACS Nano 14 (2020) 9771–9779.
[18] Q.F. Cheng, C.J. Huang, A.P. Tomsia, Freeze casting for assembling bioinspired structural materials, Adv. Mater. 29 (2017).
[19] Y. Suzawa, N. Kubo, S. Iwai, Y. Yura, H. Ohgushi, M. Akashi, Biomineral/agarose composite gels enhance proliferation of mesenchymal stem cells with osteogenic capability, Int. J. Mol. Sci. 16 (2015) 14245–14258.
[20] K. Hayashi, N. Kato, M. Kato, K. Ishikawa, Impacts of channel direction on bone tissue engineering in 3D-printed carbonate apatite scaffolds, Mater. Des. 204 (2021).
[21] T. Funayama, H. Noguchi, H. Kumagai, K. Sato, T. Yoshioka, M. Yamazaki, Unidirectional porous beta-tricalcium phosphate and hydroxyapatite artificial bone: a review of experimental evaluations and clinical applications, J. Artif. Organs 24 (2021) 103–110.
[22] A. Arora, A. Kothari, D.S. Katti, Pore orientation mediated control of mechanical behavior of scaffolds and its application in cartilage-mimetic scaffold design, J. Mech. Behav. Biomed. Mater. 51 (2015) 169–183.
[23] X.F. Wang, J. Fang, W.W. Zhu, C.X. Zhong, D.D. Ye, M.Y. Zhu, X. Lu, Y.S. Zhao, F.Z. Ren, Bioinspired highly anisotropic, ultrastrong and stiff, and osteoconductive mineralized wood hydrogel composites for bone repair, Adv. Funct. Mater. 31 (2021).
[24] S.J. Jiang, M.H. Wang, Z.Y. Wang, H.L. Gao, S.M. Chen, Y.H. Cong, L. Yang, S.M. Wen, D.D. Cheng, J.C. He, S.H. Yu, Radially porous nanocomposite scaffolds with enhanced capability for guiding bone regeneration in vivo, Adv. Funct. Mater. 32 (2022).
[25] M.H. Wu, F.X. Chen, P. Wu, Z.Q. Yang, S. Zhang, L.F. Xiao, Z.M. Deng, C. Zhang, Y. Chen, L. Cai, Bioinspired redwood-like scaffolds coordinated by in situ-generated silica-containing hybrid nanocoatings promote angiogenesis and osteogenesis both in vitro and in vivo, Adv.Healthc.Mater. 10 (2021).
[26] B.Y. Pei, Z.K. Wang, J.Y. Nie, Q.L. Hu, Highly mineralized chitosan-based material with large size, gradient mineral distribution and hierarchical structure, Carbohydrate Polym. 208 (2019) 336–344.
[27] S.J. Wang, D. Jiang, Z.Z. Zhang, Y.R. Chen, Z.D. Yang, J.Y. Zhang, J.J. Shi, X. Wang, J.K. Yu, Biomimetic nanosilica-collagen scaffolds for in situ bone regeneration: toward a cell-free, one-step surgery, Adv. Mater. 31 (2019).
[28] X. Cai, L. Chen, T. Jiang, X.Y. Shen, J.M. Hu, H. Tong, Facile synthesis of anisotropic porous chitosan/hydroxyapatite scaffolds for bone tissue engineering, J. Mater. Chem. 21 (2011) 12015–12025.
[29] K. Rezwan, Q.Z. Chen, J.J. Blaker, A.R. Boccaccini, Biodegradable and bioactive porous polymer/inorganic composite scaffolds for bone tissue engineering, Biomaterials 27 (2006) 3413–3431.
[30] H. Amani, H. Arzaghi, M. Bayandori, A.S. Dezfuli, H. Pazoki-Toroudi, A. Shafiee, L. Moradi, Controlling cell behavior through the design of biomaterial surfaces: a focus on surface modification techniques, Adv. Mater. Interfac. 6 (2019).
[31] Y.Y. Du, J.L. Guo, J.L. Wang, A.G. Mikos, S.M. Zhang, Hierarchically designed bone scaffolds: from internal cues to external stimuli, Biomaterials (2019) 218.
[32] R.A. Perez, G. Mestres, Role of pore size and morphology in musculo-skeletal tissue regeneration, Mater. Sci. Eng., C Mater.Biol. Appl. 61 (2016) 922–939.
[33] S.H. Oh, I.K. Park, J.M. Kim, J.H. Lee, In vitro and in vivo characteristics of PCL scaffolds with pore size gradient fabricated by a centrifugation method, Biomaterials 28 (2007) 1664–1671.
[34] C.Y. Xu, F. Yang, S. Wang, S. Ramakrishna, In vitro study of human vascular endothelial cell function on materials with various surface roughness, J. Biomed. Mater. Res. 71A (2004) 154–161.
[35] D. Al Mahrouqi, J. Vinogradov, M.D. Jackson, Zeta potential of artificial and natural calcite in aqueous solution, Adv. Colloid Interface Sci. 240 (2017) 60–76.
[36] M.H. Chen, Y.T. Sun, Y.H. Hou, Z. Luo, M.H. Li, Y.J. Wei, M.W. Chen, L. Tan, K.Y. Cai, Y. Hu, Constructions of ROS-responsive titanium-hydroxyapatite implant for mesenchymal stem cell recruitment in peri-implant space and bone formation in osteoporosis microenvironment, Bioact. Mater. 18 (2022) 56–71.
[37] X.C. Wu, O. Gauntlett, T.F. Zhang, S. Suvarnapathaki, C. McCarthy, B. Wu, G. Camci-Unal, Eggshell microparticle reinforced scaffolds for regeneration of critical sized cranial defects, ACS Appl. Mater. Interfaces 13 (2021) 60921–60932.
[38] X.C. Wu, S.I. Stroll, D. Lantigua, S. Suvarnapathaki, G. Camci-Unal, Eggshell particle-reinforced hydrogels for bone tissue engineering: an orthogonal approach, Biomater. Sci. 7 (2019) 2675–2685.
[39] A.K. Gaharwar, I. Singh, A. Khademhosseini, Engineered biomaterials for in situ tissue regeneration, Nat. Rev. Mater. 5 (2020) 686–705.
[40] M.S. Park, Y.H. Kim, Y. Jung, S.H. Kim, J.C. Park, D.S. Yoon, S.-H. Kim, J.W. Lee, In situ recruitment of human bone marrow-derived mesenchymal stem cells using chemokines for articular cartilage regeneration, Cell Transplant. 24 (2015) 1067–1083.
[41] J. Sun, C. Mou, Q. Shi, B. Chen, X. Hou, W. Zhang, X. Li, Y. Zhuang, J. Shi, Y. Chen, J. Dai, Controlled release of collagen-binding SDF-1 alpha from the collagen scaffold promoted tendon regeneration in a rat Achilles tendon defect model, Biomaterials 162 (2018) 22–33.
[42] A. Barhanpurkar-Naik, S.T. Mhaske, S.T. Pote, K. Singh, M.R. Wani, Interleukin-3 enhances the migration of human mesenchymal stem cells by regulating expression of CXCR4, Stem Cell Res. Ther. 8 (2017).
[43] A.L. Ponte, E. Marais, N. Gallay, A. Langonne, B. Delorme, O. Herault, P. Charbord, J. Domenech, The in vitro migration capacity of human bone marrow mesenchymal stem cells: comparison of chemokine and growth factor chemotactic activities, Stem Cell. 25 (2007) 1737–1745.
[44] Q. Zhang, J.W. Hwang, J.H. Oh, C.H. Park, S.H. Chung, Y.S. Lee, J.H. Baek, H.M. Ryoo, K.M. Woo, Effects of the fibrous topography-mediated macrophage phenotype transition on the recruitment of mesenchymal stem cells: an in vivo study, Biomaterials 149 (2017) 77–87.
[45] Q. Lu, J. Diao, Y. Wang, J. Feng, F. Zeng, Y. Yang, Y. Kuang, N. Zhao, Y. Wang, 3D printed pore morphology mediates bone marrow stem cell behaviors via RhoA/ROCK2 signaling pathway for accelerating bone regeneration, Bioact. Mater. 26 (2023) 413–424.
[46] D.D. Yao, Y.G. Lv, A cell-free difunctional demineralized bone matrix scaffold enhances the recruitment and osteogenesis of mesenchymal stem cells by promoting inflammation resolution, Biomater.Adv. 139 (2022).
[47] P. Ma, H.T. Liu, P. Wei, Q.S. Xu, X.F. Bai, Y.G. Du, C. Yu, Chitosan oligosaccharides inhibit LPS-induced over-expression of IL-6 and TNF-alpha in RAW264.7 macrophage cells through blockade of mitogen-activated protein kinase (MAPK) and PI3K/Akt signaling pathways, Carbohydrate Polym. 84 (2011) 1391–1398.
[48] L.T. Wang, P. Hu, H. Jiang, J.H. Zhao, J. Tang, D.J. Jiang, J.X. Wang, J.L. Shi, W.T. Jia, Mild hyperthermia-mediated osteogenesis and angiogenesis play a critical role in magnetothermal composite-induced bone regeneration, Nano Today 43 (2022).
[49] K. Hayashi, T. Yanagisawa, R. Kishida, K. Ishikawa, Effects of scaffold shape on bone regeneration: tiny shape differences affect the entire system, ACS Nano 16 (2022) 11755–11768.
[50] H.J. Zhang, C. Qin, M. Zhang, Y.H. Han, J.G. Ma, J.F. Wu, Q.Q. Yao, C.T. Wu, Calcium silicate nanowires-containing multicellular bioinks for 3D bioprinting of neural-bone constructs, Nano Today 46 (2022).